

Cite this: *Inorg. Chem. Front.*, 2018, 5, 1707

NiCo₂O₄/MnO₂ core/shell arrays as a binder-free catalytic cathode for high-performance lithium–oxygen cells†

Cong Tang,^{‡a} Yangjun Mao,^{‡a} Jian Xie,^{‡a,b} Zhen Chen,^c Jian Tu,^c Gaoshao Cao^b and Xinbing Zhao^{‡a,b}

Lithium–oxygen (or Li–air) cells have attracted increasing interest in recent years due to their extremely high theoretical energy density. A reasonable design of the catalytic cathode is essential to realize a high performance of Li–O₂ cells. In this work, a unique core–shell MnO₂@NiCo₂O₄ array cathode with a porous structure has been deposited directly on carbon cloth by a facile hydrothermal route. The array structure facilitates electrode wetting and oxygen gas transportation. The porous structure supplies free space for Li₂O₂ loading. The MnO₂@NiCo₂O₄ array cathode exhibits a high catalytic effect enabling the conformal growth of Li₂O₂ with the array structure retained. This growth behavior of Li₂O₂ makes the decomposition of Li₂O₂ easy upon charging. Li–O₂ cells with the MnO₂@NiCo₂O₄ cathode can sustain a stable cycling of 168 cycles with a limited capacity of 500 mA h g^{−1} at 400 mA g^{−1}, which is superior to those with the NiCo₂O₄ cathode.

Received 23rd January 2018,

Accepted 13th May 2018

DOI: 10.1039/c8qi00062j

rs.c.li/frontiers-inorganic

Introduction

Li–O₂ (or Li–air) cells have recently received great attention because of their extremely high theoretical energy density which considerably exceeds that of state-of-the-art lithium-ion cells.^{1–8} However, many challenges should be overcome before the practical applications of the Li–O₂ cells.^{9–11} One of the critical problems is the sluggish oxygen reduction/evolution reaction (ORR/OER) kinetics, which is caused by the formation/decomposition of insulating/insoluble Li₂O₂, leading to high polarization, poor rate capability and short cycle life.^{12,13} The use of catalysts has proven to be an effective strategy to improve the ORR/OER kinetics in Li–O₂ cell systems.^{14–17} Among various candidates, metal oxides, such as MnO₂,^{2,18,19} Co₃O₄,^{20,21} NiO,²² NiCo₂O₄²³ and TiO₂,²⁴ have attracted special interest since they are efficient in catalyzing

the ORR/OER and are chemically/electrochemically stable towards reactive Li₂O₂/LiO₂. In addition, they are cost-effective compared with noble metal-based catalysts.

Unlike the Li-ion shuttle mechanism in Li-ion cells, the operation of Li–O₂ cells is based on the deposition of Li₂O₂ on the cathode, which inevitably causes the deactivation of the cathode by blocking the pathways for charge transfer.^{12,13} As a result, the Li–O₂ cells usually exhibit large polarization and lower capacity than expected. Building an array-type electrode provides a practical route to improve the electrochemical performance of Li–O₂ cells since the space between the arrays can accommodate Li₂O₂, thus relieving the electrode deactivation.^{20,24,25–29} Moreover, the array-type catalysts are usually directly grown on the current collector, avoiding the binder and conducting agent-related side reactions.^{30,31} For the array-type cathodes, it is desirable that Li₂O₂ shows a conformal growth on the catalyst surface to achieve as high deposition amount as possible. However, this growth mode will easily block the catalytically active sites with the covering of insulating Li₂O₂.^{32,33}

Compared with NiO or Co₃O₄,^{34,35} NiCo₂O₄ has a high electronic conductivity, and has been widely used as the electrode material for electrocatalysis,³⁶ supercapacitors^{37–39} and Li–O₂ cells.^{23,40,41} In addition, NiCo₂O₄ can be directly grown on the conductive substrate such as Ni and carbon matrix.^{23,41} In this work, the NiCo₂O₄ nanowire arrays were directly grown on carbon cloth by a facile hydrothermal route. The NiCo₂O₄ nanowires then act as templates to grow δ-MnO₂, leading to

^aState Key Laboratory of Silicon Materials, School of Materials Science and Engineering, Zhejiang University, Hangzhou 310027, P. R. China.

E-mail: xiejian1977@zju.edu.cn; Fax: +86-571-87952181; Tel: +86-571-87951451

^bKey Laboratory of Advanced Materials and Applications for Batteries of Zhejiang Province, Hangzhou 310027, P. R. China

^cLI-FUN Technology Corporation Limited, Zhuzhou 412000, P. R. China

†Electronic supplementary information (ESI) available: Voltage profiles of Li cells with the NiCo₂O₄ cathode in Ar and O₂, Li–O₂ cells with MnO₂@NiCo₂O₄ and NiCo₂O₄ cathodes in a wide electrochemical window, LSV of Li–O₂ cells with MnO₂@NiCo₂O₄ and NiCo₂O₄ cathodes, and SEM image of the MnO₂@NiCo₂O₄ cathode after 168 cycles. See DOI: 10.1039/c8qi00062j

‡These authors contributed equally to this work.

the formation of core/shell $\text{MnO}_2@ \text{NiCo}_2\text{O}_4$ nanowires. For MnO_2 , $\delta\text{-MnO}_2$ was selected because it is a highly efficient catalyst for the ORR/OER¹⁸ and it usually crystallizes into a two-dimensional (2D) sheet-like structure with a large specific surface area.³⁴ Li-O_2 cells with the $\text{MnO}_2@ \text{NiCo}_2\text{O}_4$ cathode demonstrate a long cycle life due to the good catalytic activity of $\text{MnO}_2@ \text{NiCo}_2\text{O}_4$ and array-type electrode design. This work will shed light on the design of high-performance catalysts for advanced Li-O_2 cells.

Experimental section

Electrode preparation

The NiCo_2O_4 nanowire arrays were grown directly on carbon cloth (Shanghai Hesen Electric Co., Ltd) by a facile hydrothermal method. The precursor solution for NiCo_2O_4 growth was prepared by mixing 0.29 mg of $\text{Co}(\text{NO}_3)_2 \cdot 6\text{H}_2\text{O}$, 0.145 mg of $\text{Ni}(\text{NO}_3)_2 \cdot 6\text{H}_2\text{O}$ and 0.36 mg of $\text{CO}(\text{NH}_2)_2$ in 30 mL of de-ionized (DI) water and absolute ethanol (1 : 1 in volume) under vigorous stirring. The mixed solution with a piece of the carbon cloth (2.5 cm \times 2.5 cm) immersed was sealed into a Teflon-lined stainless steel autoclave (50 mL in capacity) which was placed in an electric oven. The hydrothermal reaction was conducted at 80 °C for 16 h. The carbon cloth with deposits was then collected, rinsed with DI water and absolute ethanol repeatedly, and dried first at 60 °C in air overnight and then at 300 °C in air for 2 h. The mass loading of NiCo_2O_4 on carbon cloth is 0.35 mg cm^{-2} . The weight of NiCo_2O_4 can be determined by the weight gain of the large-sized carbon cloth (2.5 cm \times 2.5 cm) before and after NiCo_2O_4 deposition using a precise balance. For the subsequent $\delta\text{-MnO}_2$ growth, the precursor solution was prepared by dissolving 10 mg of KMnO_4 in 50 mL DI water in a beaker (100 mL in capacity). The above carbon cloth was immersed in the KMnO_4 solution which was placed in the electric oven and heated at 90 °C for 2.5 h. After this, the carbon cloth with deposits was collected, rinsed with DI water and absolute ethanol repeatedly, and dried at 60 °C in air overnight. The final product, the carbon cloth-supported $\text{MnO}_2@ \text{NiCo}_2\text{O}_4$, was obtained after heating the above product at 300 °C in air for 2 h. The mass loading of $\delta\text{-MnO}_2$ on carbon cloth is 0.45 mg cm^{-2} . The weight of $\delta\text{-MnO}_2$ was determined by measuring the molar ratio of Mn to Co by inductively coupled plasma-atomic emission spectrometry (ICP-AES) on an IRIS Intrepid II XSP system.

Electrode characterization

X-ray diffraction (XRD) patterns of the electrodes were recorded on a Rigaku D/Max-2550pc powder diffractometer equipped with monochromatized $\text{Cu K}\alpha$ radiation ($\lambda = 1.541 \text{ \AA}$). The morphologies of $\text{MnO}_2@ \text{NiCo}_2\text{O}_4$ or NiCo_2O_4 electrodes or electrode components in different charge/discharge states were characterized by field-emission scanning electron microscopy (SEM) on a Hitachi (Japan) S-4800 microscope. The microstructure of pristine and discharged $\text{MnO}_2@ \text{NiCo}_2\text{O}_4$ was analyzed by transmission electron microscopy (TEM) on a JEM 2100F microscope.

Electrochemical measurements

Coin-type Li-O_2 cells were fabricated in an Ar-filled glove box using lithium foil ($\geq 99.9\%$, Sinopharm Chemical Reagent Co., Ltd) as the anode, carbon cloth-supported $\text{MnO}_2@ \text{NiCo}_2\text{O}_4$ (or NiCo_2O_4) as the cathode, and a Celgard C480 film as the separator. The electrolyte used is 1 M LiClO_4 ($\geq 99.99\%$, Sigma Aldrich) in tetraethylene glycol dimethyl ether (TEGDME, $\geq 99.0\%$, Sigma Aldrich). The cathodes were dried at 80 °C in a vacuum oven overnight before the fabrication of the cells. The assembled cells were purged with pure O_2 for 20 min and rested at open circuit voltage (OCV) for 5 h before the electrochemical tests. Galvanostatic cycling was carried out on a Neware battery cycler (Shenzhen, China) over a voltage range of 2.0–4.5 V (vs. Li/Li^+). For the $\text{MnO}_2@ \text{NiCo}_2\text{O}_4$ electrodes, the specific capacity (mA h g^{-1}) and current density (mA g^{-1}) of the cells were normalized to the total mass of NiCo_2O_4 and $\delta\text{-MnO}_2$. For the NiCo_2O_4 electrodes, the specific capacity and current density of the cells were normalized to the mass of NiCo_2O_4 . Cyclic voltammetry (CV) measurements were carried out on a Princeton Applied Research Versa-STAT3 electrochemistry workstation between 2.0 and 4.5 V (vs. Li/Li^+) at 0.05 mV s^{-1} . Linear sweep voltammetry (LSV) measurements were performed on the Versa-STAT3 electrochemistry workstation at a sweep rate of 0.1 mV s^{-1} . All of the electrochemical measurements were performed at 25 °C.

Results and discussion

NiCo_2O_4 nanowire arrays were grown directly on carbon cloth by a facile hydrothermal route. The XRD patterns shown in Fig. 1a indicate the formation of NiCo_2O_4 (JCPDS: no. 20-0718). MnO_2 was grown on the NiCo_2O_4 -loaded carbon cloth also by a hydrothermal route. The XRD patterns shown in Fig. 1b suggest that MnO_2 is $\delta\text{-MnO}_2$ (JCPDS: no. 80-1098), which usually crystallizes into a sheet-like layered structure,^{42,43} favorable for Li_2O_2 loading.

Fig. 2a and b show the SEM images of NiCo_2O_4 nanowires on carbon cloth. The NiCo_2O_4 nanowires were uniformly deposited on the surface of the carbon cloth (Fig. 2a). The enlarged view shown in Fig. 2b indicates that the NiCo_2O_4 nanowires have a length of 1–2 μm and a diameter of 30–60 nm with sharp tips. The SEM image also reveals that the surface of the NiCo_2O_4 nanowires is smooth. After the $\delta\text{-MnO}_2$ growth, the diameter of the nanowires increases with the array structure retained (Fig. 2c), indicating that core-shell nanowire arrays have formed. The image shown in Fig. 2d demonstrates that after the MnO_2 growth, the diameter of the nanowires increases to 100–150 nm, while the length remains almost unchanged. Unlike the smooth NiCo_2O_4 surface, the surface of $\text{MnO}_2@ \text{NiCo}_2\text{O}_4$ becomes porous, where the 2D $\delta\text{-MnO}_2$ nanosheets have assembled into a three-dimensional porous structure (Fig. 2e). This structure is desirable since the voids in the porous arrays provide the free space for Li_2O_2 deposition. The TEM image shown in Fig. 2f confirms that the nanowires exhibit a core-shell structure with a sheet-like surface. Fig. 2g

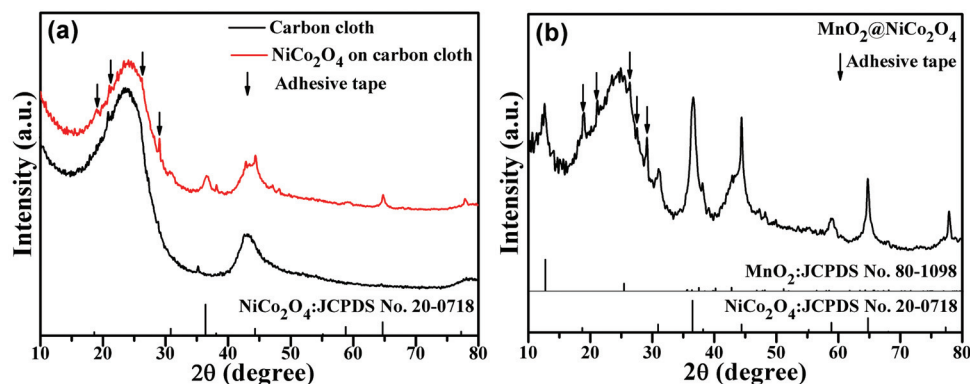


Fig. 1 XRD patterns of (a) NiCo_2O_4 and (b) $\text{MnO}_2@/\text{NiCo}_2\text{O}_4$ on carbon cloth.

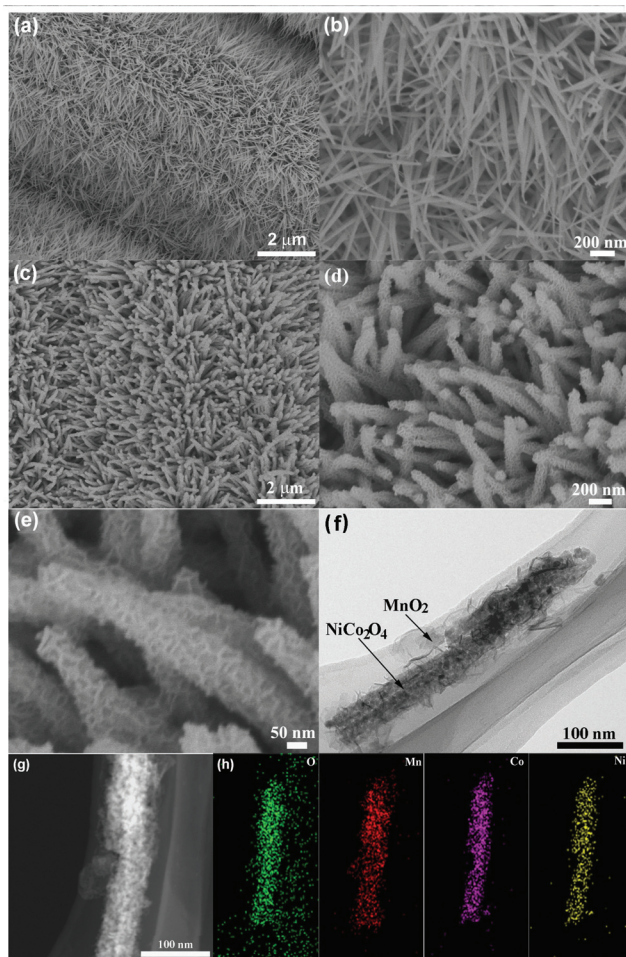


Fig. 2 SEM images of (a, b) NiCo_2O_4 and (c–e) $\text{MnO}_2@/\text{NiCo}_2\text{O}_4$ on carbon cloth, (f) TEM image of a single $\text{MnO}_2@/\text{NiCo}_2\text{O}_4$ wire, (g) HAADF-STEM image, and (h) EDS mapping of the single wire.

and h show high-angle annular dark-field (HAADF)-scanning transmission electron microscopy (STEM) images and the corresponding energy dispersive X-ray spectrometry (EDX) mapping, which further proves the core-shell structure. In

Fig. 2h, the additional O signal comes from the carbon film. From the XRD, SEM and TEM results, it is verified that core-shell structured $\text{MnO}_2@/\text{NiCo}_2\text{O}_4$ arrays have formed.

The catalytic ability of the catalysts for the ORR/OER was evaluated by galvanostatic cycling the Li– O_2 cells with the $\text{MnO}_2@/\text{NiCo}_2\text{O}_4$ or NiCo_2O_4 cathodes. Fig. 3 compares the voltage profiles of the cells with the $\text{MnO}_2@/\text{NiCo}_2\text{O}_4$ cathode and Li anode tested in O_2 and Ar. When tested in Ar, it is a common Li cell. Note that in Ar, the cell shows a low discharge capacity of below 200 mA h g^{-1} , while in O_2 , the cell (Li– O_2 cell) can yield a much higher discharge capacity of 1723 mA h g^{-1} . The result suggests that the Li-insertion into $\delta\text{-MnO}_2$ contributes minor to total capacity when the cell was tested in O_2 . For the NiCo_2O_4 cathode, the Li-insertion contribution to the total capacity is also minor as seen in Fig. S1 (ESI).† Fig. 3b and c show the voltage profiles and cycling performance of the NiCo_2O_4 -catalyzed Li– O_2 cell at 400 mA g^{-1} with a limited capacity of 500 mA h g^{-1} . The cycling of the cell lasts 66 cycles before the discharge capacity is lower than 500 mA h g^{-1} . The cell suffers from progressive polarization upon cycling due to factors such as Li corrosion by the electrolyte, electrolyte decomposition, and degradation of catalytic performance of the catalyst.^{44–46} As seen in Fig. S2,† at a high charge voltage, a voltage plateau appears due to the decomposition of the electrolyte.³¹ On the other hand, NiCo_2O_4 will react with Li ions to form Co/Ni and Li_2O at low voltage,⁴⁷ which leads to the structural destruction of NiCo_2O_4 . In addition, the theoretical working voltage of the Li– O_2 cell is 2.96 V for Li_2O_2 formation. Therefore, the cut-off voltage was set at 2–4.5 V to avoid or reduce the side reactions.

Fig. 3d and e show voltage profiles and cycling performance of the $\text{MnO}_2@/\text{NiCo}_2\text{O}_4$ -catalyzed Li– O_2 cell at 400 mA g^{-1} with a limited capacity of 500 mA h g^{-1} . The cell with the $\text{MnO}_2@/\text{NiCo}_2\text{O}_4$ cathode can sustain a stable cycling of 168 cycles, much longer than the cell with the NiCo_2O_4 cathode. At the same cycle number (66 cycles), the charge terminal voltage of the $\text{MnO}_2@/\text{NiCo}_2\text{O}_4$ -catalyzed cell is 4.25 V, which is lower than that of the NiCo_2O_4 -catalyzed cell (4.34 V), although the former has a higher catalyst loading than that of the latter, indicating a higher catalytic activity of $\text{MnO}_2@/\text{NiCo}_2\text{O}_4$ com-

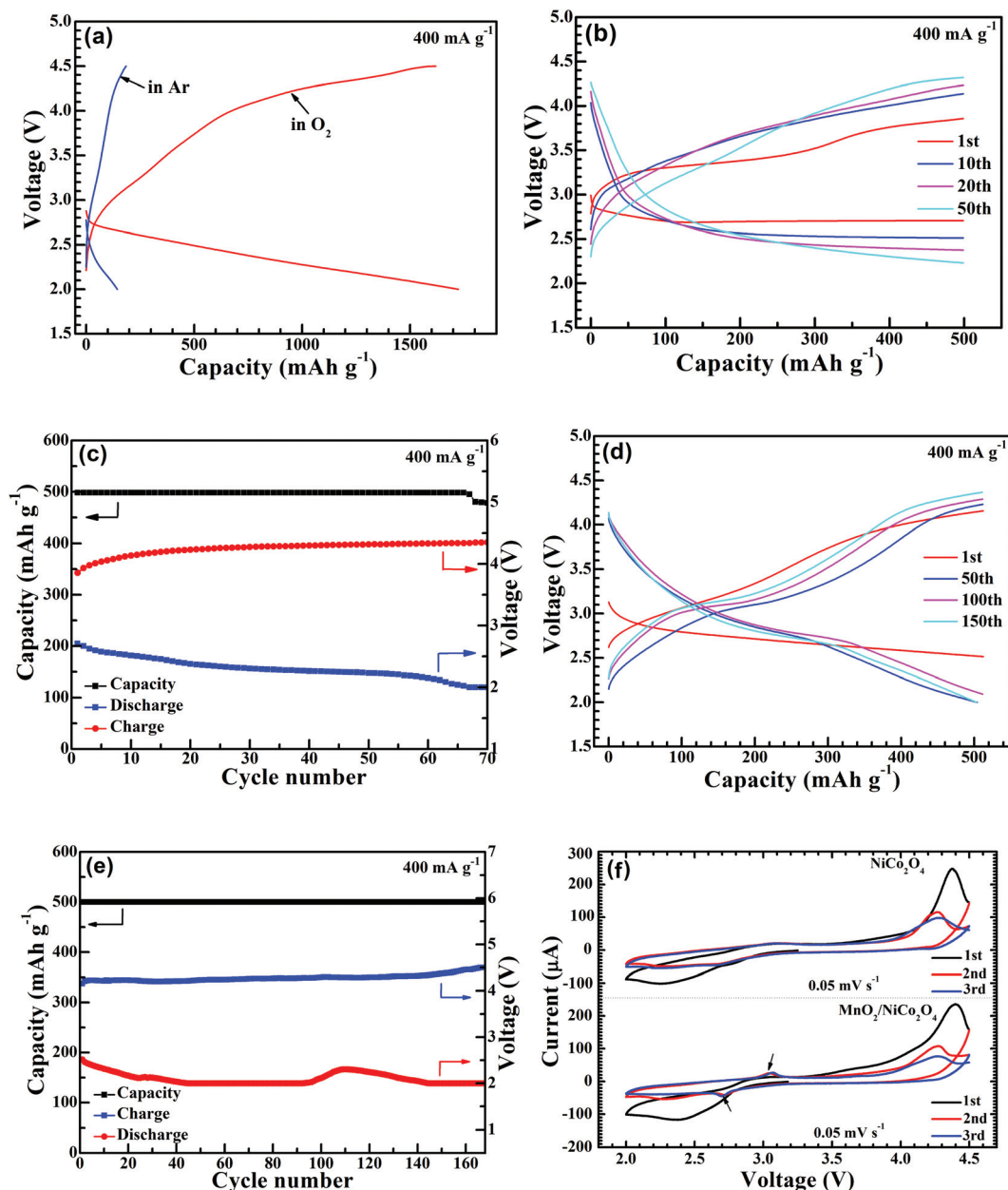


Fig. 3 (a) Voltage profiles of the Li cells with the MnO₂@NiCo₂O₄ cathode tested in O₂ and Ar, and voltage profiles and cycling performance of Li-O₂ cells with (b, c) NiCo₂O₄ and (d, e) MnO₂@NiCo₂O₄ catalysts, and CV plots of MnO₂@NiCo₂O₄ and NiCo₂O₄.

pared with that of NiCo₂O₄. The long cycle life of the Li-O₂ cell with the MnO₂@NiCo₂O₄ cathode can be attributed to the good catalytic performance of MnO₂@NiCo₂O₄, a unique array-type and porous structure of the cathode, and the binder-free cathode design. In addition, the exposure of the carbon cloth substrate to Li₂O₂ (or LiO₂) is largely minimized with the conformal growth of Li₂O₂ as discussed below. We notice that the Li-O₂ cell with MnO₂@NiCo₂O₄ shows a larger ratio of discharge capacity above 2.96 V (equilibrium potential of Li-O₂ cells) than that of the cell with NiCo₂O₄. It can be attributed to the residual cell polarization without the rest time during charge and discharge processes,⁴⁸ with a relatively low elec-

tronic conductivity of MnO₂@NiCo₂O₄. As shown in Table 1, the electrochemical performance of our MnO₂@NiCo₂O₄-catalyzed Li-O₂ cell is better than or comparable to those with the NiCo₂O₄-based catalyst when comprehensively considering the capacity limitation, applied current density and cycle life. The good electrochemical performance of our Li-O₂ cell with the MnO₂@NiCo₂O₄ catalyst is due to the presence of highly efficient δ-MnO₂ and the unique array-type binder-free electrode design with a porous structure. As seen in Fig. 3f, the CV plots of the two Li-O₂ cells exhibit similar shapes. However, for the cell with the MnO₂@NiCo₂O₄ catalyst, a couple of current peaks (marked by the black arrows) can be observed,

Table 1 Cycling performance of some Li–O₂ cells with NiCo₂O₄-based catalysts

Sample	Current density	Capacity limitation	Cycle number	Ref.
MnO ₂ @NiCo ₂ O ₄ arrays	400 mA g _{catalyst} ⁻¹	500 mA h g _{catalyst} ⁻¹	168	This work
Wave-like NiCo ₂ O ₄	100 mA g _{catalyst} ⁻¹	500 mA h g _{catalyst} ⁻¹	100	23
NiCo ₂ O ₄ nanotubes	200 mA g _{carbon} ⁻¹	1000 mA h g _{carbon} ⁻¹	110	40
NiCo ₂ O ₄ nanowires	30 mA g _{catalyst} ⁻¹	500 mA h g _{catalyst} ⁻¹	50	49
Mushroom-like Au/NiCo ₂ O ₄	42.5 mA g _{catalyst} ⁻¹	510 mA h g _{catalyst} ⁻¹	40	50
NiCo ₂ O ₄ nanorods	400 mA g _{carbon} ⁻¹	1000 mA h g _{carbon} ⁻¹	15	51
NiCo ₂ O ₄ nanowires	18 mA g _{catalyst} ⁻¹	500 mA h g _{catalyst} ⁻¹	13	52
NiCo ₂ O ₄ nanosheets	200 mA g _{carbon} ⁻¹	500 mA h g _{catalyst} ⁻¹	50	53
CeO ₂ @NiCo ₂ O ₄ nanowires	100 mA g _{catalyst} ⁻¹	500 mA h g _{catalyst} ⁻¹	64	54

which is related to the Li-insertion/removal into/from δ-MnO₂ and the small peak intensity agrees with its minor contribution to the total capacity of the cell. LSV measurements in Fig. S3† show that MnO₂@NiCo₂O₄ has a larger cathodic current than that of bare NiCo₂O₄, which further proves that MnO₂@NiCo₂O₄ has a better catalytic activity than that of NiCo₂O₄.

To reveal the different catalytic performances of NiCo₂O₄ and MnO₂@NiCo₂O₄ catalysts, the cathodes after discharge and charge processes were characterized by SEM as shown in Fig. 4–6. For the NiCo₂O₄ cathode, after the first discharge process, the array structure is generally preserved, indicating that the growth of Li₂O₂ shows a surface mode, namely, Li₂O₂ grows conformally on the surface of the NiCo₂O₄ nanowires. This growth mode enables the good contact between the catalyst and Li₂O₂, while the catalytically active sites will be easily blocked by the insulating Li₂O₂.^{32,33} As marked by the white arrow in Fig. 4a, large Li₂O₂ particles were also observed, which form due possibly to the loss of the active sites on NiCo₂O₄ by Li₂O₂ deposition. Besides on the surface of NiCo₂O₄ nanowires, Li₂O₂ sheets also form between the neighboring NiCo₂O₄ nanowires (Fig. 4b), which will block the pathway of electrolyte penetration and O₂ gas transportation.

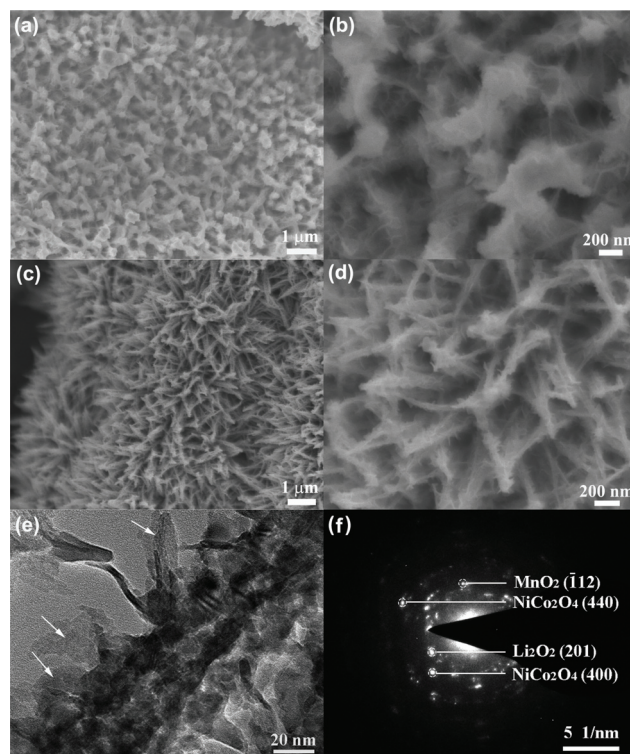


Fig. 5 SEM images of the MnO₂@NiCo₂O₄ cathodes after (a, b) the first discharge and (c, d) the first charge processes, and (e) TEM image and (f) SAED patterns of the discharged MnO₂@NiCo₂O₄.

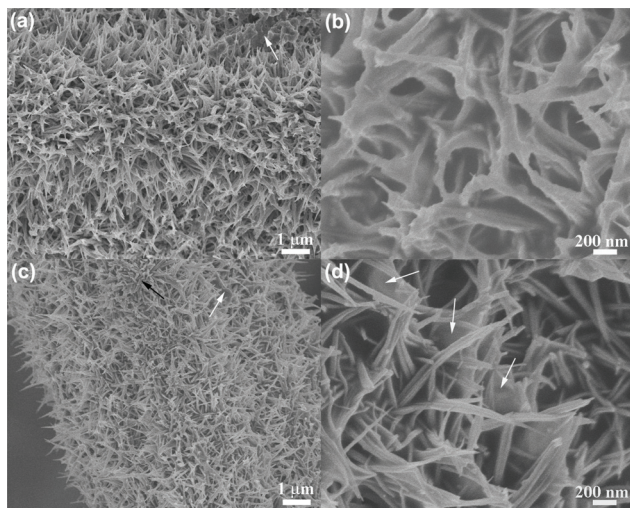


Fig. 4 SEM images of the NiCo₂O₄ cathodes after (a, b) the first discharge and (c, d) the first charge processes.

As expected, the large particles and sheets are difficult to be decomposed upon charging as marked by the white arrows in Fig. 4c and d due to the insufficient contact with the catalyst. In contrast, Li₂O₂ on the NiCo₂O₄ surface has been removed after the charge process. As shown in Fig. 4c, only after one cycle, some NiCo₂O₄ nanowires have broken (see the black arrow), which will result in the deactivation of the catalyst and the degradation of the cell performance.

Fig. 5a and b show the SEM images of the MnO₂@NiCo₂O₄ cathode after the first discharge and charge processes. Similar to NiCo₂O₄, its array structure was also retained after the first discharge process. Compared with that of the pristine nanowires (Fig. 2c), the diameter of MnO₂@NiCo₂O₄ after the discharge process increases while the voids between the nanowires are still visible, suggesting that Li₂O₂ also adopts a

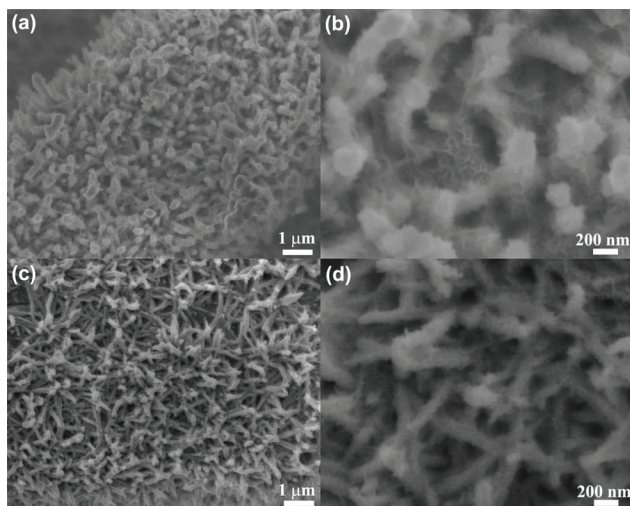


Fig. 6 SEM images of the $\text{MnO}_2@ \text{NiCo}_2\text{O}_4$ cathodes after (a, b) the 50th discharge and (c, d) the 50th charge processes.

surface-growth mode. $\delta\text{-MnO}_2$ is usually rich in defects and has abundant oxygen vacancies,⁵⁵ which act as the catalytically active centers to promote the formation of LiO_2 on the surface during the early ORR stage. Li_2O_2 adopts a surface growth mode through the reaction $\text{LiO}_2 + \text{Li}^+ + \text{e}^- \rightarrow \text{Li}_2\text{O}_2$ as the ORR proceeds with the strong absorption of LiO_2 with $\delta\text{-MnO}_2$ and the synergetic catalytic effect of NiCo_2O_4 and $\delta\text{-MnO}_2$. In addition, the porous structure assembled by sheet-like $\delta\text{-MnO}_2$ facilitates this surface growth mode. As seen in Fig. 5b, the original porous structure is invisible due to the filling of the pores with Li_2O_2 . No large Li_2O_2 particles form since there is large space in porous $\text{MnO}_2@ \text{NiCo}_2\text{O}_4$ for housing Li_2O_2 . In addition, thin sheets are also observed between the discharged $\text{MnO}_2@ \text{NiCo}_2\text{O}_4$ nanowires. However, voids between the $\text{MnO}_2@ \text{NiCo}_2\text{O}_4$ nanowires are still present for barrier-free O_2 transportation and electrolyte penetration. After the charge step, the diameter of the nanowires decreases with the porous structure appearing again, which suggests the sufficient removal of Li_2O_2 after the charge process (Fig. 5c and d). The TEM image shown in Fig. 5e also indicates that the diameter of the nanowire increases after the discharge process. The discharged product is confirmed to be Li_2O_2 by selected area electron diffraction (SAED) as shown in Fig. 5f. After 50 cycles, the array structure is generally maintained. This can explain the relatively durable catalytic activity of the $\text{MnO}_2@ \text{NiCo}_2\text{O}_4$ cathode and long cycle life of the Li– O_2 cell. However, morphological changes have occurred which may underlie the performance degradation of the cell. As discussed above, since Li_2O_2 adopts a conformal growth mode, repetitive loading/unloading of Li_2O_2 will induce stress within $\text{MnO}_2@ \text{NiCo}_2\text{O}_4$, leading to the progressive damage of the structure and accompanied degradation of the catalytic performance. As seen in Fig. S4,[†] after 168 cycles, the array-structure of $\text{MnO}_2@ \text{NiCo}_2\text{O}_4$ has almost been destroyed and large particles can be observed even after the charge process. This indicates

that the byproducts are accumulated after long-time cycling. The electrochemical performance of the cell will thus deteriorate and the cell failure finally occurs. As a result, these *ex situ* SEM characterization studies agree well with the electrochemical performance of the Li– O_2 cells.

Conclusions

In summary, we propose a unique design of a core-shell $\text{MnO}_2@ \text{NiCo}_2\text{O}_4$ array-type cathode without using the binder. In this design, the array-type structure is favorable for electrode wetting by the electrolyte and oxygen gas transportation. The porous structure of MnO_2 makes high Li_2O_2 loading possible even though it adopts a conformal growth mode. The conformal growth of Li_2O_2 on $\text{MnO}_2@ \text{NiCo}_2\text{O}_4$ enables its easy decomposition upon charging. The binder-free electrode design and the conformal growth of Li_2O_2 also exclude (or minimize) the side reactions related to the binder and carbon cloth substrate. As a result, Li– O_2 cells catalyzed by $\text{MnO}_2@ \text{NiCo}_2\text{O}_4$ exhibit good cycling stability (168 cycles with a limited capacity of 500 mA h g^{-1}). This work provides a new design of an efficient catalytic cathode for Li– O_2 cells.

Conflicts of interest

There are no conflicts to declare.

Acknowledgements

This work was supported by the National Natural Science Foundation of China (No. 51572238) and the Strategic Emerging Industry Project of Hunan Province on the development and application of low-cost sodium ion energy-storage batteries (2016GK4030).

References

- 1 K. M. Abraham and Z. Jiang, *J. Electrochem. Soc.*, 1996, **143**, 1–5.
- 2 T. Ogasawara, A. Débart, M. Holzapfel, P. Novák and P. G. Bruce, *J. Am. Chem. Soc.*, 2006, **128**, 1390–1393.
- 3 P. G. Bruce, S. A. Freunberger, L. J. Hardwick and J. M. Tarascon, *Nat. Mater.*, 2012, **12**, 19–29.
- 4 Z. Q. Peng, S. A. Freunberger, Y. H. Chen and P. G. Bruce, *Science*, 2012, **337**, 563–566.
- 5 A. C. Luntz and B. D. McCloskey, *Chem. Rev.*, 2014, **114**, 11721–11750.
- 6 N. Imanishi and O. Yamamoto, *Mater. Today*, 2014, **17**, 24–30.
- 7 L. Grande, E. Paillard, J. Hassoun, J. B. Park, Y. J. Lee, Y. K. Sun, S. Passerini and B. Scrosati, *Adv. Mater.*, 2105, 27, 784–800.
- 8 D. Aurbach, B. D. McCloskey, L. F. Nazar and P. G. Bruce, *Nat. Energy*, 2016, **1**, 16128.

- 9 Y. Y. Shao, F. Ding, J. Xiao, J. Zhang, W. Xu, S. Park, J. G. Zhang, Y. Wang and J. Liu, *Adv. Funct. Mater.*, 2013, **23**, 987–1004.
- 10 L. H. Ye, W. Q. Lv, J. Y. Cui, Y. C. Liang, P. Wu, X. N. Wang, H. He, S. J. Lin, W. Wang, J. H. Dickersons and W. D. He, *ChemElectroChem*, 2015, **2**, 312–323.
- 11 N. N. Feng, P. He and H. S. Zhou, *Adv. Energy Mater.*, 2016, **6**, 1502303.
- 12 V. Viswanathan, K. S. Thygesen, J. S. Hummelshøj, J. K. Nørskov, G. Girishkumar, B. D. McCloskey and A. C. Luntz, *J. Chem. Phys.*, 2011, **135**, 214704.
- 13 O. Gerbig, R. Merkle and J. Maier, *Adv. Mater.*, 2013, **25**, 3129–3133.
- 14 Z. W. Chang, J. J. Xu, Q. C. Liu, L. Li and X. B. Zhang, *Adv. Energy Mater.*, 2015, **5**, 1500633.
- 15 Z. Ma, X. X. Yuan, L. Li, Z. F. Ma, D. P. Wilkinson, L. Zhang and J. J. Zhang, *Energy Environ. Sci.*, 2015, **8**, 2144–2198.
- 16 Z. Y. Wen, C. Shen and Y. Lu, *ChemPlusChem*, 2015, **80**, 270–287.
- 17 X. Guo, B. Sun, D. W. Su, X. X. Liu, H. Liu, Y. Wang and G. X. Wang, *Sci. Bull.*, 2017, **62**, 442–452.
- 18 S. Y. Liu, Y. G. Zhu, J. Xie, Y. Huo, H. Y. Yang, T. J. Zhu, G. S. Cao, X. B. Zhao and S. C. Zhang, *Adv. Energy Mater.*, 2014, **4**, 1301960.
- 19 Y. X. Hu, T. R. Zhang, F. Y. Cheng, Q. Zhao, X. P. Han and J. Chen, *Angew. Chem., Int. Ed.*, 2015, **54**, 4338–4343.
- 20 Y. M. Cui, Z. Y. Wen and Y. Liu, *Energy Environ. Sci.*, 2011, **4**, 4727–4734.
- 21 J. Z. Zhu, X. D. Ren, J. J. Liu, W. Q. Zhang and Z. Y. Wen, *ACS Catal.*, 2015, **5**, 73–81.
- 22 S. F. Tong, M. B. Zheng, Y. Lu, Z. X. Lin, J. Li, X. P. Zhang, Y. Shi, P. He and H. S. Zhou, *J. Mater. Chem. A*, 2015, **3**, 16177–16182.
- 23 C. Shen, Z. Y. Wen, F. Wang, K. Rui, Y. Lu and X. W. Wu, *J. Power Sources*, 2015, **294**, 593–601.
- 24 Q. C. Liu, J. J. Xu, D. Xu and X. B. Zhang, *Nat. Commun.*, 2015, **6**, 7892.
- 25 Y. Q. Chang, S. M. Dong, Y. H. Ju, D. D. Xiao, X. H. Zhou, L. X. Zhang, X. Chen, C. Q. Shang, L. Gu, Z. Q. Peng and G. L. Cui, *Adv. Sci.*, 2015, **2**, 1500092.
- 26 S. T. Kim, N. S. Choi, S. Park and J. Cho, *Adv. Energy Mater.*, 2015, **5**, 1401030.
- 27 J. Y. Cao, S. Y. Liu, J. Xie, S. C. Zhang, G. S. Cao and X. B. Zhao, *ACS Catal.*, 2015, **5**, 241–245.
- 28 F. F. Tu, Q. N. Wang, J. Xie, G. S. Cao, S. C. Zhang, J. W. Wang, S. X. Mao, X. B. Zhao and H. Y. Yang, *Energy Storage Mater.*, 2017, **6**, 164–170.
- 29 W. B. Luo, T. V. Pham, H. P. Guo, H. K. Liu and S. X. Dou, *ACS Nano*, 2017, **11**, 1747–1754.
- 30 R. Black, S. H. Oh, J. H. Lee, T. Yim, B. Adams and L. F. Nazar, *J. Am. Chem. Soc.*, 2012, **134**, 2902–2905.
- 31 M. M. Ottakam Thotiyil, S. A. Freunberger, Z. Q. Peng and P. G. Bruce, *J. Am. Chem. Soc.*, 2013, **135**, 494–500.
- 32 S. Lau and L. A. Archer, *Nano Lett.*, 2015, **15**, 5995–6002.
- 33 J. W. Wang, Y. L. Zhang, L. M. Guo, E. K. Wang and Z. Q. Peng, *Angew. Chem., Int. Ed.*, 2016, **55**, 1–6.
- 34 T. Y. Wei, C. H. Chen, H. C. Chien, S. Y. Lu and C. C. Hu, *Adv. Mater.*, 2010, **22**, 347–351.
- 35 L. Shen, L. Yu, X. Y. Yu, X. Zhang and X. W. Lou, *Angew. Chem., Int. Ed.*, 2015, **54**, 1868–1872.
- 36 H. Hu, B. Y. Guan, B. Y. Xia and X. W. Lou, *J. Am. Chem. Soc.*, 2015, **137**, 5590–5595.
- 37 L. Yu, G. Q. Zhang, C. Z. Yuan and X. W. Lou, *Chem. Commun.*, 2013, **49**, 137–139.
- 38 X. F. Lu, D. J. Wu, R. Z. Li, Q. Li, S. H. Ye, Y. X. Tong and G. R. Li, *J. Mater. Chem. A*, 2014, **2**, 4706–4713.
- 39 F. X. Ma, L. Yu, C. Y. Xu and X. W. Lou, *Energy Environ. Sci.*, 2016, **9**, 862–866.
- 40 L. Y. Li, L. F. Shen, P. Nie, G. Pang, J. Wang, H. S. Li, S. Y. Dong and X. G. Zhang, *J. Mater. Chem. A*, 2015, **3**, 24309–24314.
- 41 G. X. Liu, L. Zhang, S. Q. Wang, L. X. Ding and H. H. Wang, *J. Mater. Chem. A*, 2017, **5**, 14530–14536.
- 42 Y. F. Li, S. C. Zhu and Z. P. Liu, *J. Am. Chem. Soc.*, 2016, **138**, 5371–5379.
- 43 J. B. Zhu, Q. Y. Li, W. T. Bi, L. F. Bai, X. D. Zhang, J. F. Zhou and Y. Xie, *J. Mater. Chem. A*, 2013, **1**, 8154–8159.
- 44 R. S. Assary, J. Lu, P. Du, X. Y. Luo, X. Y. Zhang, Y. Ren, L. A. Curtiss and K. Amine, *ChemSusChem*, 2013, **6**, 51–55.
- 45 R. Younesi, M. Hahlin, F. Björefors, P. Johansson and K. Edström, *Chem. Mater.*, 2013, **25**, 77–84.
- 46 X. H. Yao, Q. Dong, Q. M. Cheng and D. W. Wang, *Angew. Chem., Int. Ed.*, 2016, **55**, 11344–11353.
- 47 Y. M. Wang, J. Li, S. Chen, B. Li, G. P. Zhu, F. Wang and Y. X. Zhang, *Inorg. Chem. Front.*, 2018, **5**, 559–567.
- 48 G. Q. Wang, L. L. Huang, S. Y. Liu, J. Xie, S. C. Zhang, P. Y. Zhu, G. S. Cao and X. B. Zhao, *ACS Appl. Mater. Interfaces*, 2015, **7**, 23876–23884.
- 49 C. Shen, Z. Y. Wen, F. Wang, X. W. Wu and C. H. Chen, *JOM*, 2016, **68**, 2585–2592.
- 50 F. F. Tu, J. Xie, S. C. Zhang, G. S. Cao, T. J. Zhu and X. B. Zhao, *J. Mater. Chem. A*, 2015, **3**, 5714–5721.
- 51 B. Sun, J. Q. Zhang, P. Munroe, H. J. Ahn and G. X. Wang, *Electrochem. Commun.*, 2013, **31**, 88–91.
- 52 W. M. Liu, T. T. Gao, Y. Yang, Q. Sun and Z. W. Fu, *Phys. Chem. Chem. Phys.*, 2013, **15**, 15806–15810.
- 53 B. Sun, X. D. Huang, S. Q. Chen, Y. F. Zhao, J. Q. Zhang, P. Munroe and G. X. Wang, *J. Mater. Chem. A*, 2014, **2**, 12053–12059.
- 54 Z. D. Yang, Z. W. Chang, J. J. Xu, X. Y. Yang and X. B. Zhang, *Sci. China: Chem.*, 2017, **12**, 1540–1545.
- 55 Y. X. Zhao, C. Chang, F. Teng, Y. F. Zhao, G. B. Chen, R. Shi, G. I. N. Waterhouse, W. F. Huang and T. R. Zhang, *Adv. Energy Mater.*, 2017, **7**, 1700005.